Optimal site selection for Choutuppal geomagnetic observatory, based on geophysical evidences

Divyanshu Dwivedi[1], Sneh Yadav[2], Kusumita Arora[1], Rakesh Murteli[1], Alok Taori[3]

[1]Geomagnetism, CSIR-National Geophysical Research Institute, India

[2]Kurukshetra University, India

[3]National Remote Sensing Centre, India

Correspondence: Divyanshu Dwivedi; email id: ddwivedigp@gmail.com

Abstract

The phases of development of the Choutuppal magnetic observatory over last 15 years has enabled the effects of the natural environment like groundwater changes and lightning activity on the magnetic data to be evaluated. A high resolution survey of total field anomalies led to the construction of the 3D model of the shallow surface. Constrained by conductivity depth slices from previous ERT and EVRI surveys, the distribution of sandy regolith, saprolite, and granitic layers in the shallow subsurface are delineated. The pattern of lightning strikes in a 10 km area around the observatory are correlated to modulations and disruptions in the magnetic data. The analysis as a whole provides information for selecting a location to install a secondary variometer room by taking into account topography, lightning effect, soil resistivity, low magnetic anomaly and distance from the recharge pond, which can produce continuous data of higher quality and consistency than at present.

Keywords: Choutuppal observatory, Magnetic anomaly, Spectral analysis, Lightning data

1. Introduction:

The Choutuppal (CPL) geo-electric observatory (Geographic coordinates: 78.920E, 17.290N; Geomagnetic coordinates: 149.24E, 7.47N) of CSIR-NGRI was established near Choutuppal town in the Nalgonda district, approximately 60 km southeast of Hyderabad city, Telangana state (Sanker Narayan, 1964). The region primarily comprises granite and gneissic formations. These rocks are part of the Peninsular Gneissic Complex, which is one of the oldest geological formations in India, dating back to the Archean era. The weathering of the granitic and gneissic rocks has led to the formation of red and lateritic soils. The granitic formation is encroached locally by discontinuities such as dikes or quartz reefs but these are not present on the site (Guihéneuf et al., 2014). The area around the CPL observatory mainly consists of alkali feldspar granite (Figure 1a). The regional geology of resistive granitic basement rocks, uniform soil cover, arid vegetation, and gentle topography for effective drainage of runoff water during rainy seasons were assessed to be suitable for geo-electric measurements (Sanker Narayan et al., 1967; Sarma et al., 1969). Below the surface, shallow drillings revealed: 1) A sandy regolith layer 0-2 m thick which is made up of sandy-clay of quartz grains, 2) A laminated saprolite layer of variable thickness of 10 - 15 m derived from in-situ weathering of granite, 3) A 15-20 m thick layer of fissured granite, where weathered granite and some clay partially fill the fissures. The effective porosity of this layer is very low and mainly due to the fissure zones (Dewandel et al., 2006; 2012).

The geo-electric measurements at CPL were based on orthogonal 500 m electric dipoles and magnetic pulsations were measured with solid core induction coils. Hourly values of the magnetic variation and analysis of equatorial magnetic pulsations were

59   reported from CPL (CSIR NGRI report, 1972). These hourly values are published in

60   the Indian magnetic data volumes and uploaded to WDC Kyoto (Svendsen et al.,

61   1990). Figure 1b shows the 105-acre star shaped campus of CSIR-NGRI in

62   Choutuppal. One high magnetic anomaly is present at the eastern part of the campus.

63   In the rest of the area, the total range is ~ 80 nT. The surface topography is least in

64   the east and north and higher is the west and southern part of the campus. Several

65   shallow boreholes drilled in the northern end are used for hydrogeological studies in

66   fractured hard rock terrains. These studies monitored the nature of the granitic

67   basement rocks, local hydrogeology, and managed aquifer recharge (MAR) within the

68   CPL observatory, through a large, shallow lake in the eastern quadrant of the campus.

69

70   Geo-electric measurements on this campus were discontinued in 1982, but when the

71   Metro Rail project in the vicinity of the HYB magnetic observatory in Hyderabad

72   appeared to threaten its existence in 2010, the Choutuppal campus was re-visited for

73   re-location possibilities of HYB. This work summarizes the different situations, which

74   affect the operation of a low latitude magnetic observatory, some mitigation measures

75   and some unanswered questions.

76
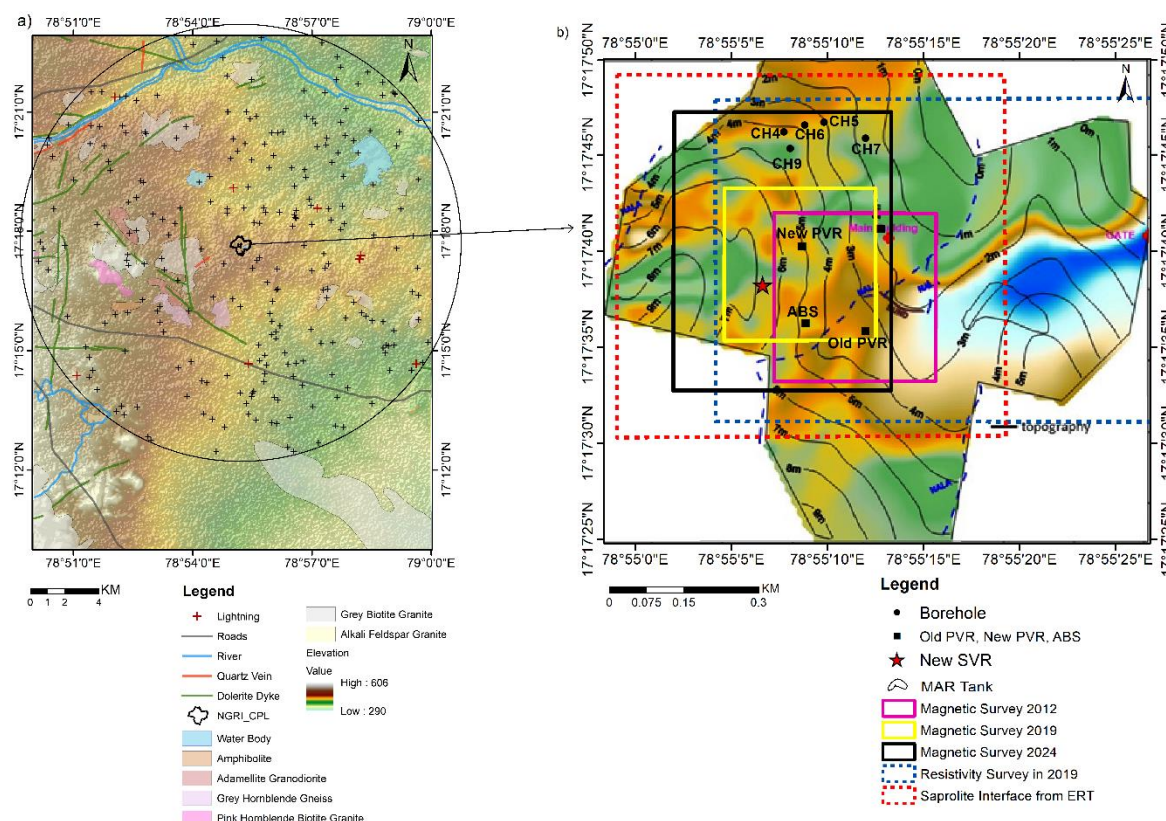
Figure 1: a) The geological map shows the area around the CSIR-NGRI- CPL observatory superimposed over topography. '+' symbols show lightning locations within a 10 km radius (circle mark) from January 2022 to August 2022 with maximum intensity 60480 amp, b) The magnetic anomaly map (after Sanker Narayan et al., 1967) is superimposed on local elevation. The locations of the magnetic and electric surveys are marked by solid and dashed rectangles. PVR=Primary variometer room, ABS= Absolute room, SVR= Secondary variometer room, MAR = managed aquifer recharge.

2. First phase of CPL Magnetic Observatory:

i) Survey of magnetic data and building CPL Observatory

Prior to establishing the observatory buildings, a magnetic survey was conducted in

November 2012 over an area of 200 m x 200 m with 20 m intervals, between the Main

Building and the southern side of the campus, marked by pink rectangle in Figure 1b,

which had the smallest anomalies as per the earlier survey. This area was sufficiently

far away from the boundary of the campus to ensure that local activities outside the

campus may not have significant contribution to the measurements. The total

96   magnetic anomaly range (Figure 2) was ~ 150nT with changes in magnetic field within

97   ~20 nT around proposed locations of the old PVR and ABS rooms.

98
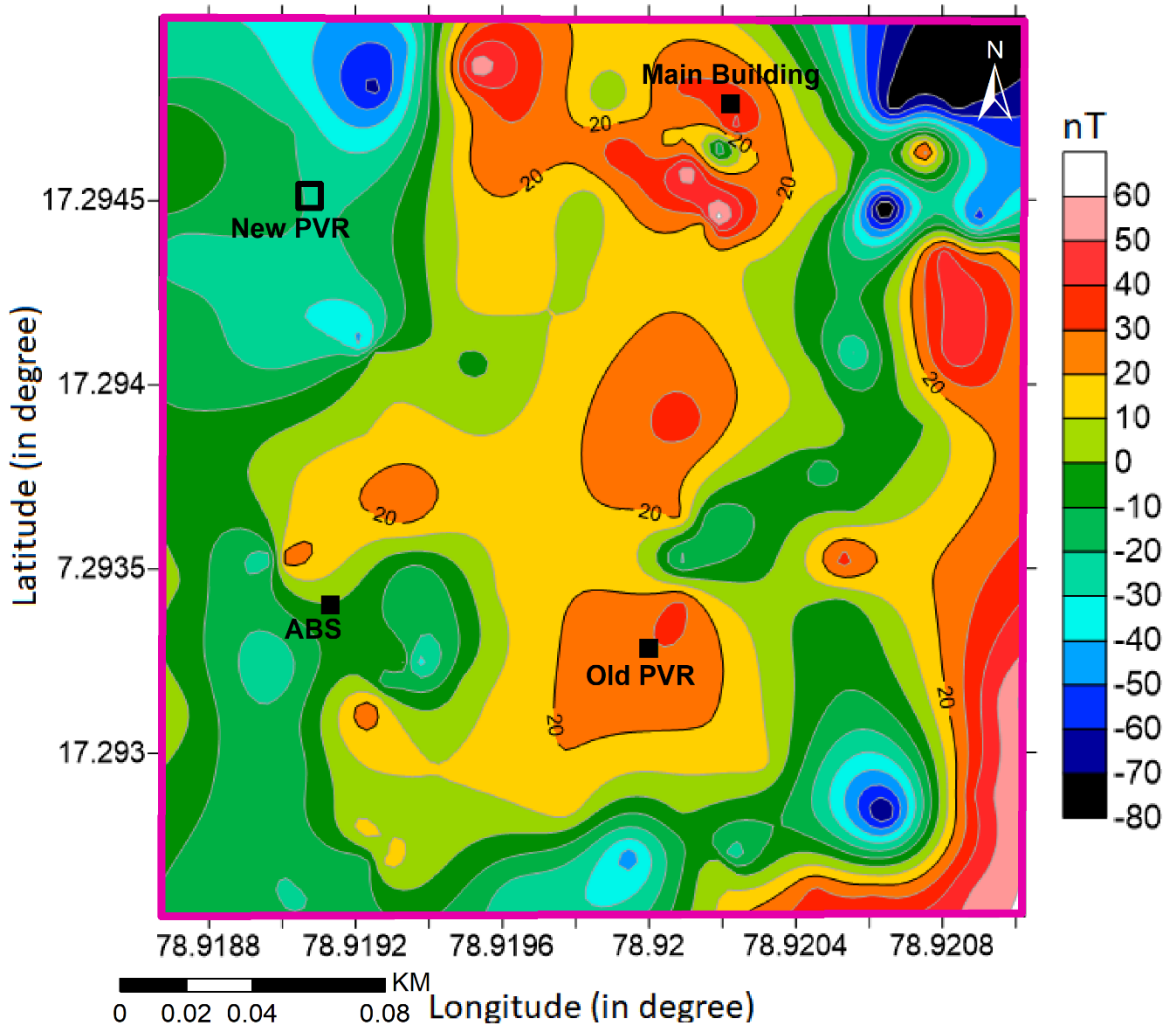
99   **Figure 2:** Magnetic anomaly plot of the survey region in 2012. Black box is the marked
100   location for the New PVR, built in 2019-2020.

101

102   In this central location the surface topography is low and a shallow water channel

103   (nalla) flows SE-NW through the area between the Old PVR and ABS. The Old PVR

104   construction (with double walled, 3.5 m underground vault) started in the June 2013

105   using non-magnetic sandstone. The ABS room was constructed on slightly elevated

106   ground with two pillars inside and four pillars outside. In April 2014, the CPL

107   observatory was commissioned, equipped with tri-axial fluxgate magnetometer and

108   Zeiss single axis fluxgate theodolite for Declination-Inclination measurements. The

109   XVII IAGA Observatory Workshop was held on these premises in October 2014 with

110   93 international participants from 33 countries. The definitive data from CPL is

111   published at INTERMAGNET, 2015 onwards.

112

113   **ii)   Hydrogeological Park and managed aquifer recharge:**

114   The region of CPL Observatory has a semi-arid climate with an average annual

115   maximum temperatures ranging as 28°C - 45°C. The mean annual rainfall is around

116   751 mm, which ranges from 2 mm in February to 171 mm in July. Water levels are

117   highly variable depending on the monsoon and usually range between 2 and 26 m

118   (meters below ground surface). Water level measurements at the northern part of the

119   Choutuppal campus has been monitored since 1999 in two dozen boreholes, some of

120   them are marked in Figure 1b, by the Indo-French Center for Groundwater Research

121   (IFCGR) (Maréchal et al, 2018) to study the hydrodynamic properties and associated

122   hydrological processes in crystalline aquifers. As part of a governmental scheme of

123   strengthening groundwater through recharge state-wise MAR projects, an infiltration

124   basin was dug in Choutuppal (marked in black outline as MAR in Figure 1b) in 2015

125   to meet the demands of farmers in the area facing water scarcity. The basin has

126   dimensions of 120 m × 40 m, with a depth of about 2 m, effectively removing the

127   regolith layer and extending into the saprolite. The basin is mainly supplied by a canal

128   which diverts water from the Musi River (Nicolas et al., 2019; Maurya et al., 2021).

129   Nicolas et al (2019) has shown that intra-seasonal groundwater fluctuations have only

130   moderate response to rainfall patterns, which could be due to usage trends as well as

131   hydraulic permittivity parameters. After the MAR basin filling, groundwater levels rose

132   by 6 m in one year. Figure 3a shows the water level changes of five boreholes (CH5,

CH4, CH6, CH7, and CH9) before and after monsoon from 2011 to 2023 with a data gap during 2021-22. While it is clear that most of the time water level lies at intermediate depth of ~ 10 to 30 m, individually, CH5 and CH7 show the least seasonal fluctuations over the years, CH6, CH4 and CH9 show variations of 20 m or more; possibly very local fracture properties facilitate vertical flow of water. Starting from April 2017, the water levels in the boreholes rose significantly, coming almost to surface in September 2017 and reducing a little by July 2018. In December 2023, the water levels recorded are nearly similar to that of September 2017. It can be inferred that sustained water in the MAR basin has allowed the shallow aquifers to be permanently recharged. In September 2017, the rainfall of the monsoon combined with prevalent saturated condition led to the flooding of the Old PVR vault (Figure 3c). The water level receded by a few metre the following summer but did not fall to earlier levels. While this was good news for recharge, the Old PVR was now unusable.
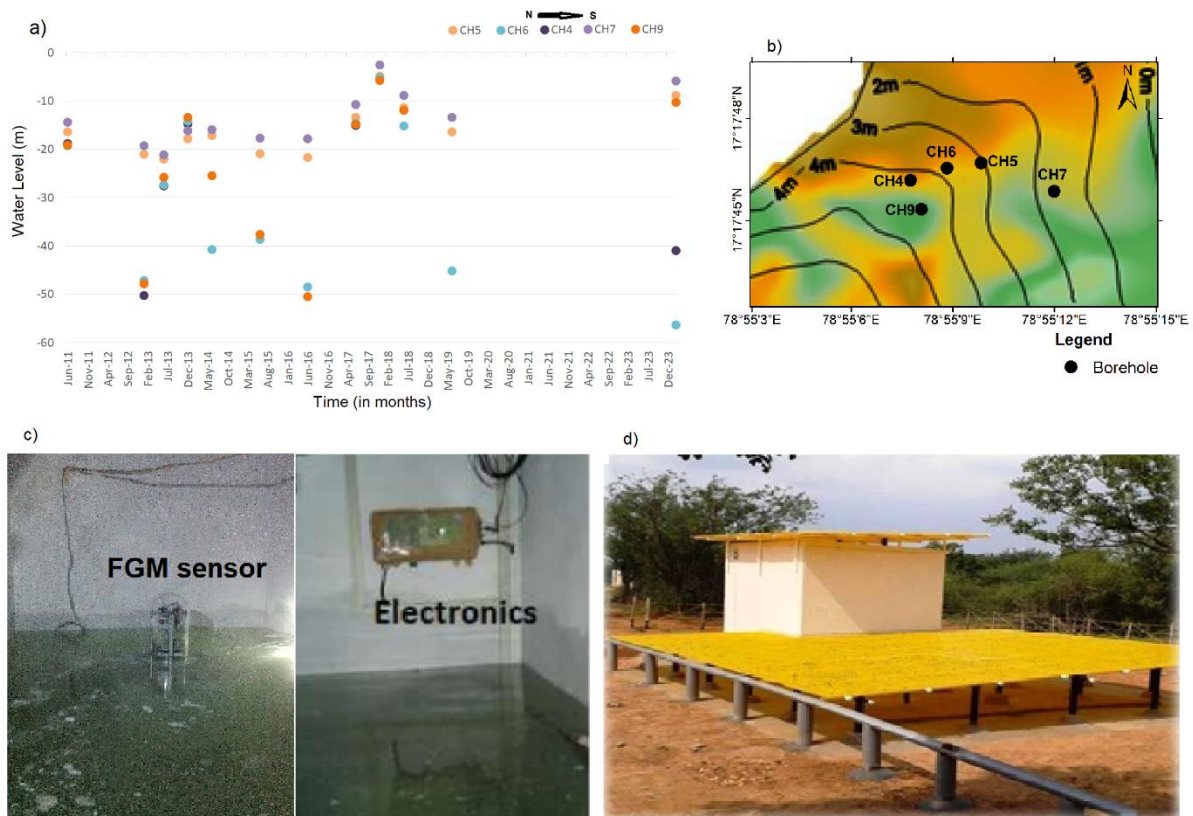
147 **Figure 3:** a) Fluctuations of water level in a few boreholes in the north of
148 Choutuppal campus, b) location of boreholes in the map, c) the submerged vault
149 in September 2017, d) the outside view of the old PVR.

150

151 ## 3. Second phase of CPL Magnetic Observatory:

152
153 ### i) Survey and commissioning of new PVR

154 With the need for a new variometer building, a fresh survey was conducted in May

155 2019 using GSM19 Overhauser magnetometers, marked by the yellow rectangle

156 in Figure 1b. This area was some tens of meter west of the earlier survey location,

157 still central to the campus, on ground which is about 2-3 m higher, which could

158 avoid the shallow groundwater conditions. This total field magnetic survey was

159 carried out during six geomagnetic quiet days in May 2019 over a 240 X 240 square

160 meter area with 10 m spacing. The magnetic anomaly of the region shows total

161 amplitude variation of ~300nT (Figure 4a) with ~10nT anomaly north of the ABS

162 room; the proposed location is marked as New PVR in Figure 4a. This time a raised

163 building with double walls and double roof was constructed of non-magnetic

164 limestone to ensure no groundwater incursion issues for the foreseeable future

165 (Figure 4b). The New PVR was commissioned in January 2021.

166

167
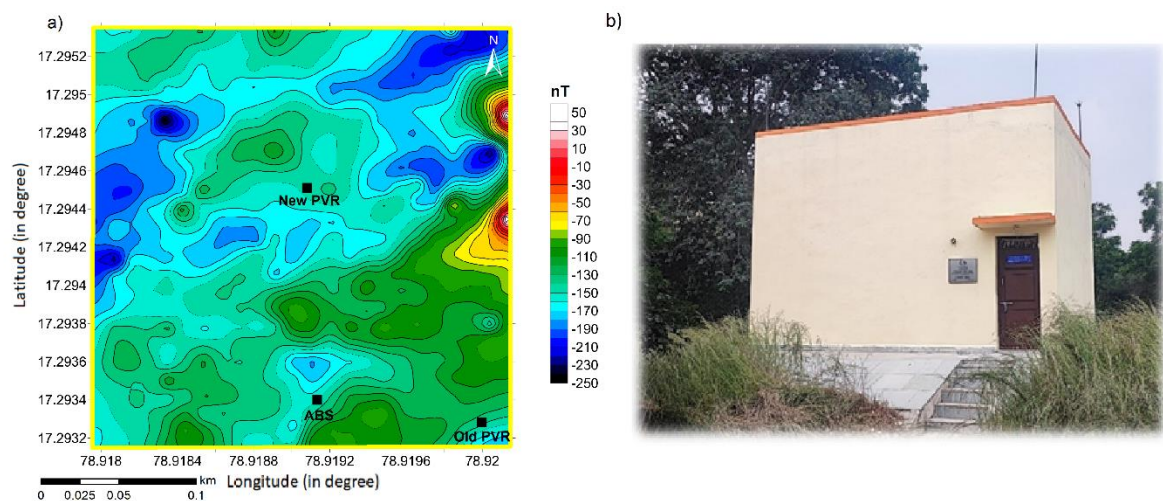
Figure 4: a) Magnetic anomaly plot of the survey region in 2019, b) New PVR building inaugurated in January 2021.

Recurrent malfunctions of the electronics (2-3 times a month) of the digital fluxgate magnetometer (DFM) recording electronics were noticed in second half of 2021 and 2022, a new phenomenon. After rounds of thorough inspections, it was suspected that lightning activity in the vicinity of the Choutuppal campus was causing the damage inspite of installation of 6 lightning arrester rods and 4 earthing pits. Being an open ground with no tall obstructions, the lightning activity in this area was found to be more frequent than around HYB observatory in Hyderabad. The earthing pits and lightning arrester system were strengthened further but only marginally countered the effects on the electronics.

ii)   **Lightning activity patterns around CPL Observatory and effects on data**

ISRO-National Remote Sensing Center (NRSC) has a network of 46 radio frequency lightning detection sensors, covering the entire part of the India (shown in Figure 5a). The Lightning detection sensor network monitors the cloud to ground lightning occurrences by virtue of emitted waves in the 5 Hz - 30 MHz range and geolocation is calculated using the time of arrival method. The detection range is upto 800 km with more than 98% confidence within 300 km range, with 50% overlap to maintain high geo-location accuracy of lightning occurrences (Taori et al., 2022; 2023). We have examined the lightning data in a radius of 10 km around CPL observatory, marked as + in Figure 1a. Figure 5b shows the shows the occurrence frequency of lightning over the months from January to August 2022; + symbols denote the instances when the lightning caused damage in the fluxgate electronics. Figure 5b shows that substantial

195   lower intensity lightning activities are recorded during January, April, May and June.

196   Surprisingly July had no lightning in the area in 2022, in August, the higher intensity

197   lightning was more numerous. Two instances of failure of the instrument electronics

198   occurred during the higher intensity lightning of April and August, whereas a

199   disturbance of May was associated with lower amplitude lightning, discussed in next

200   section.

201
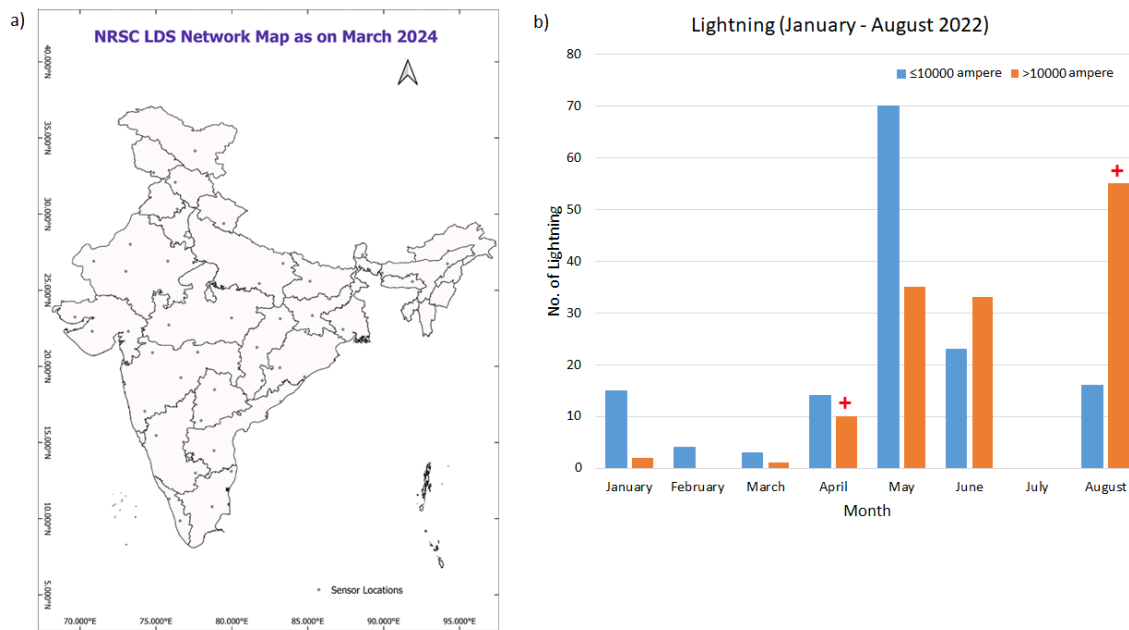
202
203   **Figure 5:** a) Map of lightning sensors in India, b) Distribution of low and high intensity
204   lightning occurrences during January to August 2022.
205

206   Examination of the H (horizontal), D (declination), and Z (vertical) components of 1-

207   sec data in LT (local time) for 04th May, 2022 data from the new PVR shows continuous

208   spikes from 7- 8.2 LT in all the components, followed by a shift of ~ 70, 20 and 150 nT

209   in H, D and Z respectively (Figure 6a). After rebooting the instrument, the data came

210   back to its normal range. Comparison with lightning data established that this

211   disturbance was due to lightning effect (correlated red mark). It is noticed that at the

212   time of 7.94 LT hour there was shift in the data which correlate with the lightening

213   intensity of 8879 and 14243 ampere at the same time (Lightning data from NRSC)

214   which strike the ground within 10 km radius of CPL campus.
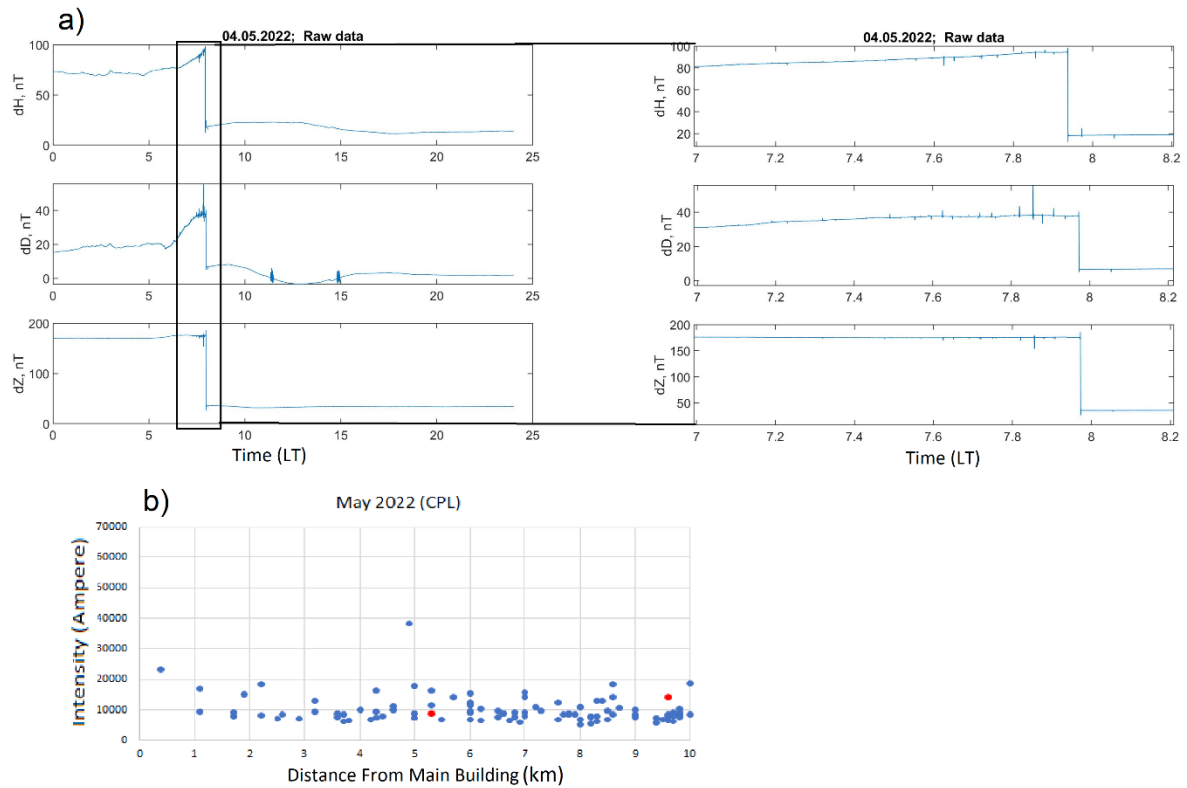
215

216   **Figure 6:** Raw data (H, D, Z component) plot for a) 04th May, 2022 at the new PVR,
217   b) plot of lightning intensity (in ampere) with distance (in km) from main building.
218

219   Further, we examined the H, D, Z components of 1-sec data in LT for the 30th April and

220   26th May, 2017 data from the Old PVR, on days which had some weather activities.

221   From the data, it is clear that there were no shifts in the data, but some continuous

222   spikes were observed from 18.0 -18.8 LT (Figure 7). The spikes are more prominent

223   in the Z component (>0.5nT). Though lighting data was not available in this duration,

224   the general conditions lead us to believe that these minor signatures were lightning

225   induced.

226
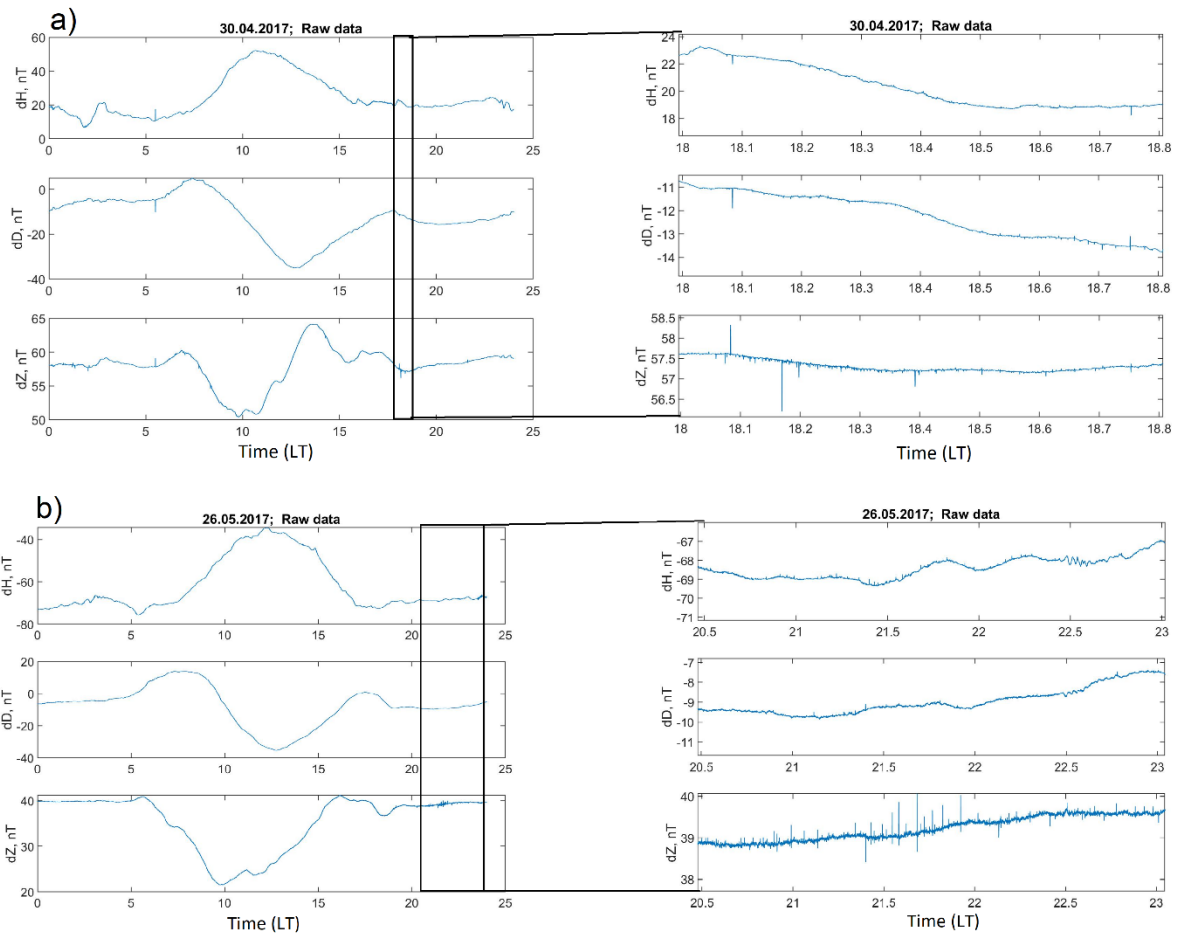
Figure 7: Raw data (H, D, Z component) plot for a) 30th April, b) 26th May, 2017 at the old PVR.

Table 1 provides examples of the amplitudes of the disturbances recorded in data vis-à-vis the light intensities and distance from the recording system

Date	Time (LT)	H	D	Z	Lightning amplitude (ampere)	Distance (km)	Remark
15-04-2022	23.2 - 24.00	0.1nT	0.2nT	1nT	20968	5.5	GSM90 stopped recording & spikes in HDZ
04-05-2022	7.0 - 8.2	70nT	20nT	150nT	8879, 14243	5.3, 10	Shift in data(HDZ)
29-08-2022	-	-	-	-	37387,24329, 21210, 8553	3.9, 5.5, 9.2, 10	DFM Stopped recording
30-04-2017	18.0 - 18.8	0.8nT	1nT	1.2nT	-	-	Spikes in HDZ
26-05-2017	20.5 -23.0	0.2nT	0.2nT	1nT	-	-	Spikes in HDZ

233   It was suspected that because the new PVR is constructed on the surface and the

234   cables were laid in the surface layer, instead of the vault configuration as in the one

235   which was flooded, the effects of lightning activity on the data has been amplified.

236   Given the fact that in future years more uncertainty and swings in climatic parameters

237   are anticipated due to effects of climate change, it was deemed necessary to conduct

238   further studies to find a location based on optimal ranges of a variety of parameters

239   like topography, distance from MAR lake, the configuration of near surface regolith and

240   saprolite layers along with groundwater conditions.

241

242   **4. New search for optimal location**

243   Higher ground away from the MAR basin can be found toward the western side of the

244   campus. In order to evaluate its suitability as a new long term location for continuous

245   magnetic measurements, this study aims to delineate the sub-surface structures using

246   the high-resolution magnetic data constrained by resistivity information conducted

247   through Electrical Resistivity Tomography (ERT) and Electrical Vector Resistivity

248   Imaging (EVRI) measurements at the Choutuppal campus and surrounding areas

249   during 2016-2017. The magnetic method can be sensitive to presence of near surface

250   variations and produce a model of these layers as well as in locating faults, folds, shear

251   zones, delineating geological structures, and groundwater contamination studies

252   (Reynolds, 1997; Hinze et al., 2013; Kumar et al., 2018; Dwivedi and Chamoli, 2021,

253   2022). We try to find out a suitable location for a new SVR (secondary variometer

254   room) where effects of lightning and groundwater level changes can be minimum in

255   the medium-to-long term.

256

257

258 **i)   2024 survey**

259 A 1-sec total magnetic field survey was conducted during February 2024 (4 days) at

260 10 m sampling intervals as same done in 2019 survey. The data of 2019 and 2024

261 were combined, thus covering a total of ~ 400x320 square meters. The diurnal and

262 International Geomagnetic Reference Field (IGRF 14) corrections are applied to the F

263 data, so that the residuals reflect only the local crustal contributions. Finally, we applied

264 the kriging interpolation method to generate the grid and produce the magnetic

265 anomaly of this area (Figure 8a). Further, this was converted by a 'reduced to equator'

266 computation to remove ambiguities in location of causative sources of magnetic

267 anomalies, at low and high latitudes. In this study, we chose the values of

268 Delineation=0°, and Inclination=24° and estimate the RTE generated magnetic

269 anomaly map of the study region. The RTE filtered map centres anomalies over their

270 sources and removes the asymmetry of the magnetic anomaly due to nonzero

271 magnetic inclination and helps in magnetic data interpretation (Figure 8b).
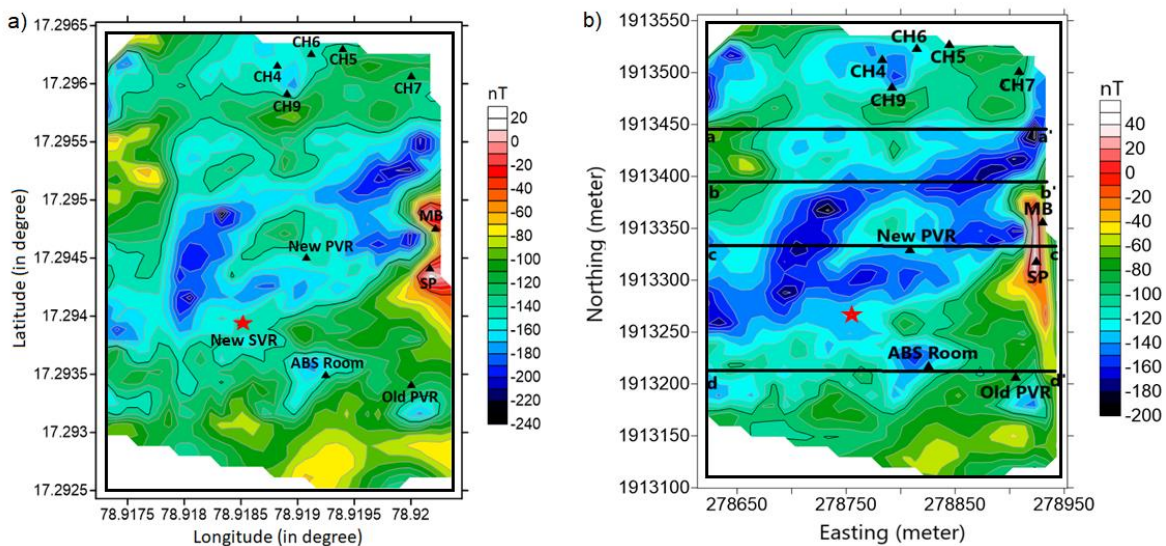
272
273
274 **Figure 8: a)** The magnetic anomaly of the study area. (MB=main building, SP= solar
275 panel, CH= bore well channels, ABS= absolute, PVR= primary variometer room, SVR=
276 secondary variometer room). Red star mark shows the proposed New SVR in the
277 region, b) the magnetic anomaly after reduction to equator of the study area. The aa',
278 bb', cc' and dd' shows four magnetic profiles modelled.

The RTE magnetic anomaly shows a variation of ~ 260 nT in the region. The low anomaly is dominant in the central part followed by the high anomaly near the main building and solar panel. The new PVR lies in the low anomaly region where the three-axis flux magnetometer is installed to record 1-sec H, D, and Z component data of Earth's magnetic field. The ABS room location is set up in the low anomaly zone to measure the Delineation-Inclination using the Mag-01 DI-fluxgate magnetometer mounted on theodolite.

We have considered four profiles aa', bb, cc', and dd' along EW in the RTE magnetic anomaly map to characterise the subsurface susceptibility model (Figure 8b). The magnetic data shows its importance in characterizing the shallow sub-surface structures, which would be further beneficial for the selection of new location to install magnetic observatory in the campus. The lightning data is considered from the National Remote Sensing Centre (NRSC), Hyderabad, India, to investigate the failure of the DFM (digital fluxgate magnetometer) electronics during the lightning strike. The high-resolution topography data is obtained from the Shuttle Radar Topography Mission (SRTM) Global 30 (https://earthexplorer.usgs.gov/) to plot the elevation of the region.

The ERT surveys for different profiles (AA', DD', EE', FF' and GG') were carried out using Wenner and Schlumberger arrays with 48 electrodes in the campus. The profiles AA', DD', EE' with 5 m unit electrode spacing achieved a maximum length of 360 m whereas FF' and GG' covers 240 m (Maurya et al, 2021). The vertical cross section along these profiles and a horizontal depth slice at a depth of 30 m below ground level

303 derived from 3D model reflect few linear conductive features and surficial resistivity

304 heterogeneities (Figure 13a).

305

306 **ii)   Analysis of subsurface source and depths**

307 The fast Fourier transform (FFT), a robust technique is used by several researchers

308 to calculate the mean depth of layered interfaces of the potential field datasets

309 (Chamoli et al., 2011, 2023; Dwivedi et al., 2019). The power spectrum analysis gives

310 the average depth of the sources with an error limit of 10% (Mishra and Pederson,

311 1982). The 2D radially averaged power spectrum of the RTE magnetic anomaly data

312 shows two linear slope segments corresponding to the average depth of two interfaces

313 around 12±1.2 m and 1±0.1 m (Figure 9).

314
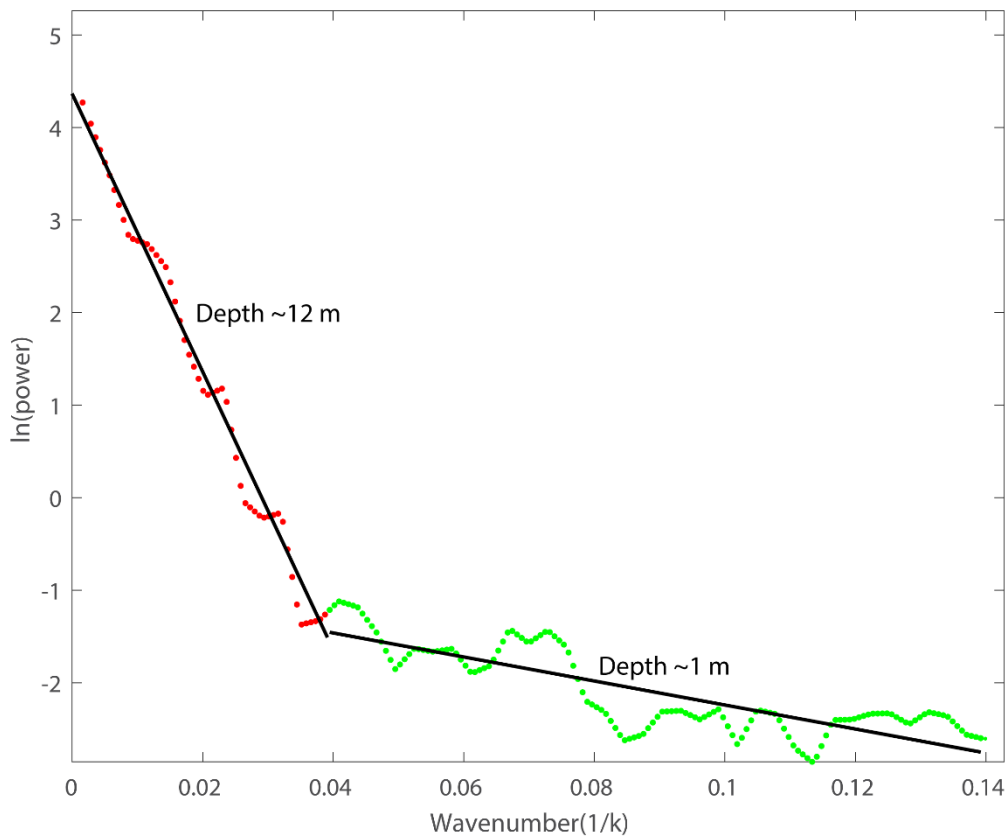
315 **Figure 9:** Radially averaged power spectrum of the RTE magnetic anomaly. Different
316 layer segment gives an average depth of layered interfaces.

317   The tilt depth is an effective method in characterizing the location of source edge as

318   well as magnetic source depth using the tilt angle (TDR) approach (Salem et al., 2007).

319   First, the TDR is described by the following equation (Miller and Singh, 1994).

320    $$\theta = tan^{-1} \left[\frac{\partial M}{\partial Z} \Bigg/ \sqrt{\left(\frac{\partial M}{\partial x}\right)^2 + \left(\frac{\partial M}{\partial y}\right)^2} \right]$$ (1)

321   where $\frac{\partial M}{\partial x}, \frac{\partial M}{\partial y}, \frac{\partial M}{\partial z}$ are the first derivative of the magnetic field M in the x, y and z

322   directions. The zero contour ($\theta = 0^0$) demarcates the spatial location of magnetic

323   source and tilt amplitudes restrict in the range of $+90^0$ to -90^0. Salem et al., (2007)

324   introduced the tilt depth technique using the relationship among tilt angle (θ), depth

325   (Z_c), horizontal location (h) of a contact as:

326    $$\theta = tan^{-1}\left[\frac{h}{Z_c}\right]$$ (2)

327   In the equation 2, the contact location ($h = 0$) lies to the zero values of the contour and

328   depth relates to the horizontal distance between the 0^0 and $\pm45^0$ contour in the TDR

329   map. We apply the technique to generate the tilt angle (TDR), tilt depth solution and

330   histogram plot on the magnetic gridded data. Figure 10 presents the TDR map with

331   displaying of contours of -45°, 0°, $+45^o$ (dashed black lines). The TDR shows the short

332   wavelength anomalies and closely spaced contours that corresponds to shallow sub

333   surface sources. The zero contour values of the TDR show the location of the source

334   whereas the half of the distance between $\pm45^o$ contours demarcates depth of the

335   sources. It can be seen that distance between 0° and $+45^0$ is demarcated by relative

336   closeness over the shallow sources and wide expanses over the deeper sources.

337

338

339

340
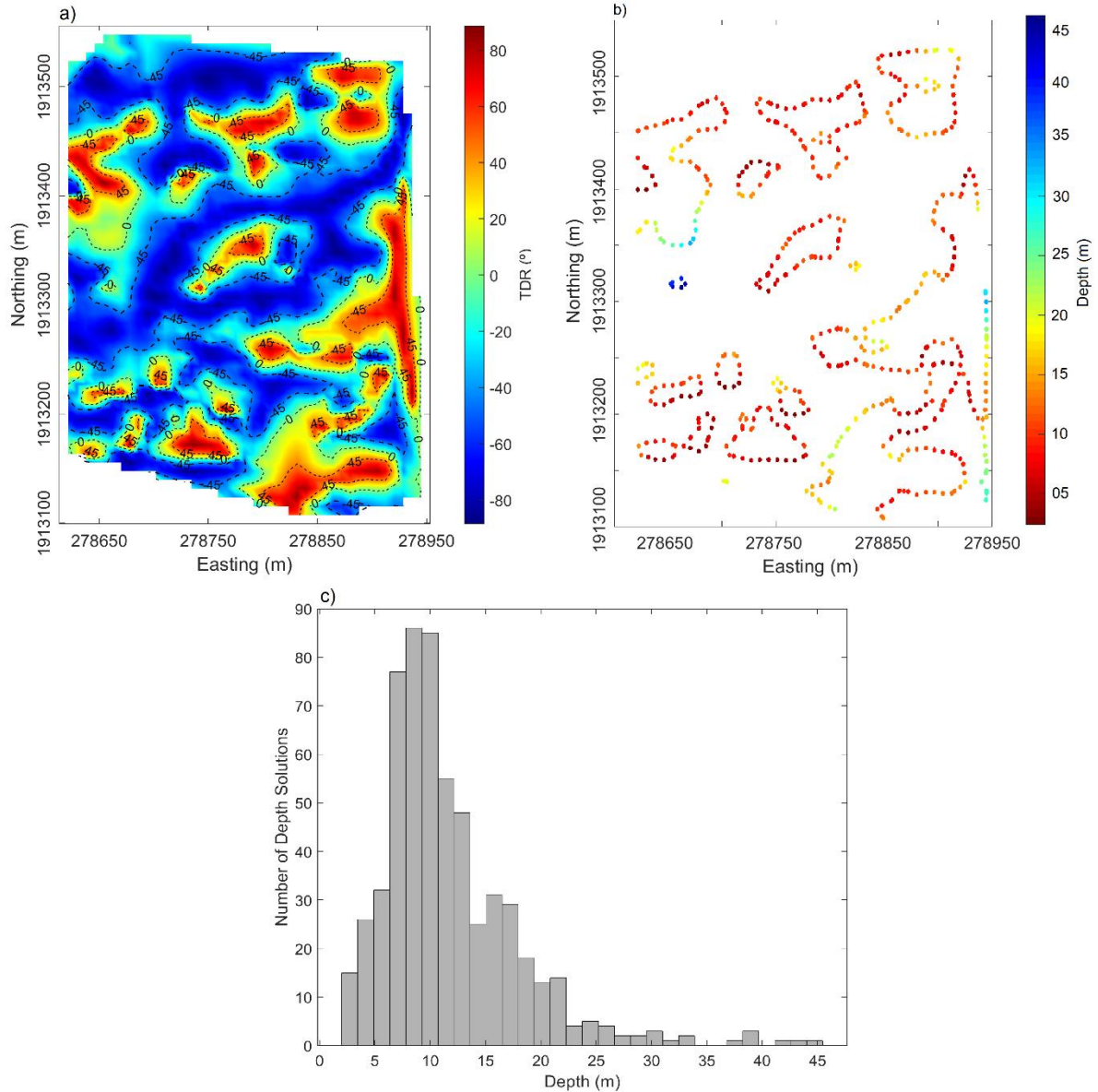
Figure 10: a) The tilt angle plot, b) The tilt depth solutions, c) the tilt depth solution histogram plot of the RTE magnetic anomaly.

The tilt depth solutions of the RTE magnetic anomaly data with depth variation from ~ 2 m to 45 m. Most of the sources lie in shallow depth ~ 2 to 20 m and extended in one direction. The histogram plot shows the variation between number of depth solution and depth (Figure 10c). It is clear from the plot that number of depth solution are maximum in the depth range of ~ 2 m to 20 m which corresponds to shallow source in the sub surface.

350

351   **iii)**   **Magnetic data inversion and forward models**

352

353   We invert the RTE magnetic anomaly to estimate the depth variation of the interface

354   with strong susceptibility contrast. We use the method of Parker (1973) which works

355   in the Fourier domain to estimate the depth variation of an undulated interface. The

356   depth of interface can be computed from the magnetic anomaly due to an uneven,

357   uniform magnetized layer by inversion procedure. The method is improved by

358   incorporating high cut filter to ensure the convergence of series and to avoid instability

359   at high wavenumber (Pham et al., 2020). Based on the power spectrum

360   characteristics, we have chosen the cut-off wavenumber between 0.038-0.13 m^{-1} to

361   remove the high frequencies. The resultant map shows that this interface is deepest

362   in the centre of the survey area and shallowest towards the edges; then present PVR

363   and the ABS Room are in the zones where this interface is deep, whereas the old

364   PVR, which was flooded was in the zone of shallow interface (Figure 11a). The

365   calculated depth is inferred as the saprolite layer, which varies from ~ 12 to 16 m with

366   a mean depth of ~14 m. Figure 11b shows the variation of the root mean square (RMS)

367   error against the iteration number. In this case, the inversion process performed 175

368   iterations, and the RMS error between two successive approximations was reduced

369   from 0.0680 m to 9.9584× 10^{-5} m.

370
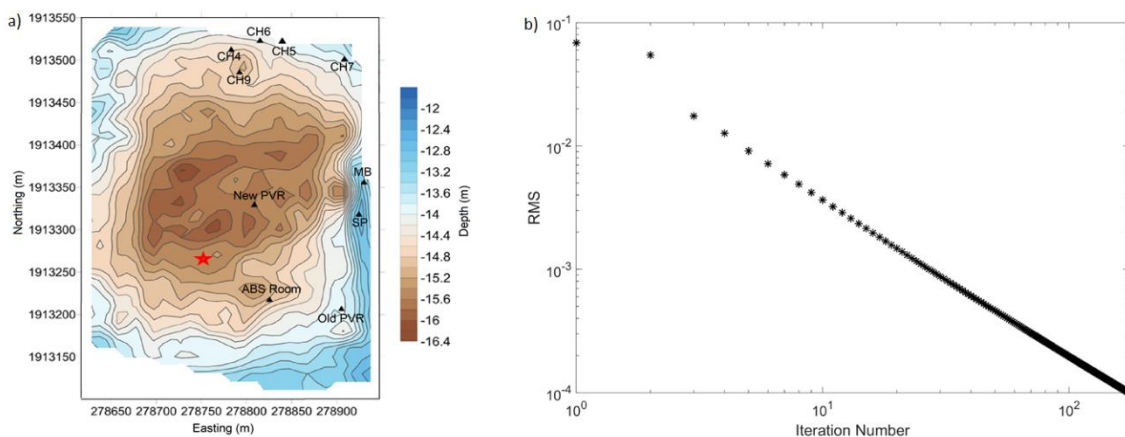
Figure 11: a) The depth variation of the saprolite interface derived from the inversion of the RTE magnetic anomaly after removing the high frequency component, b) variation of RMS error against the iteration number.

Further, we model the RTE derived magnetic anomaly data along four profiles aa', bb',

cc', and dd' (Figure 8b) to delineate the details of the sub-surface structures. The

forward modelling along these profiles is carried out using the IGMAS+ software, a

tool for forward and inverse modelling of potential field datasets (Anikiev et al., 2023).

The total length of theses profiles are ~310 m which show the depth variations up to

50 m from the surface (Figure 12a). The 2D models along these profiles explains the

presence of three layered structures from the surface up to a depth of 50 m as: sandy

regolith (~0.3 susceptibility in SI), saprolite (~3 susceptibility in SI), and fissured granite

(~2.5 susceptibility in SI). The average susceptibility value for sandy regolith layer is

measured in the field using KT-10 magnetic susceptibility meter whereas others are

referenced from Telford et al., (1990). The saprolite interface is incorporated in the

models based on previous results of ERT data (Nicolas et al., 2019). The average

thickness of the sandy regolith layer is ~3 m whereas the saprolite layer is ~ 10 m in

the models. Both the saprolite and regolith layers show undulations in the all models.
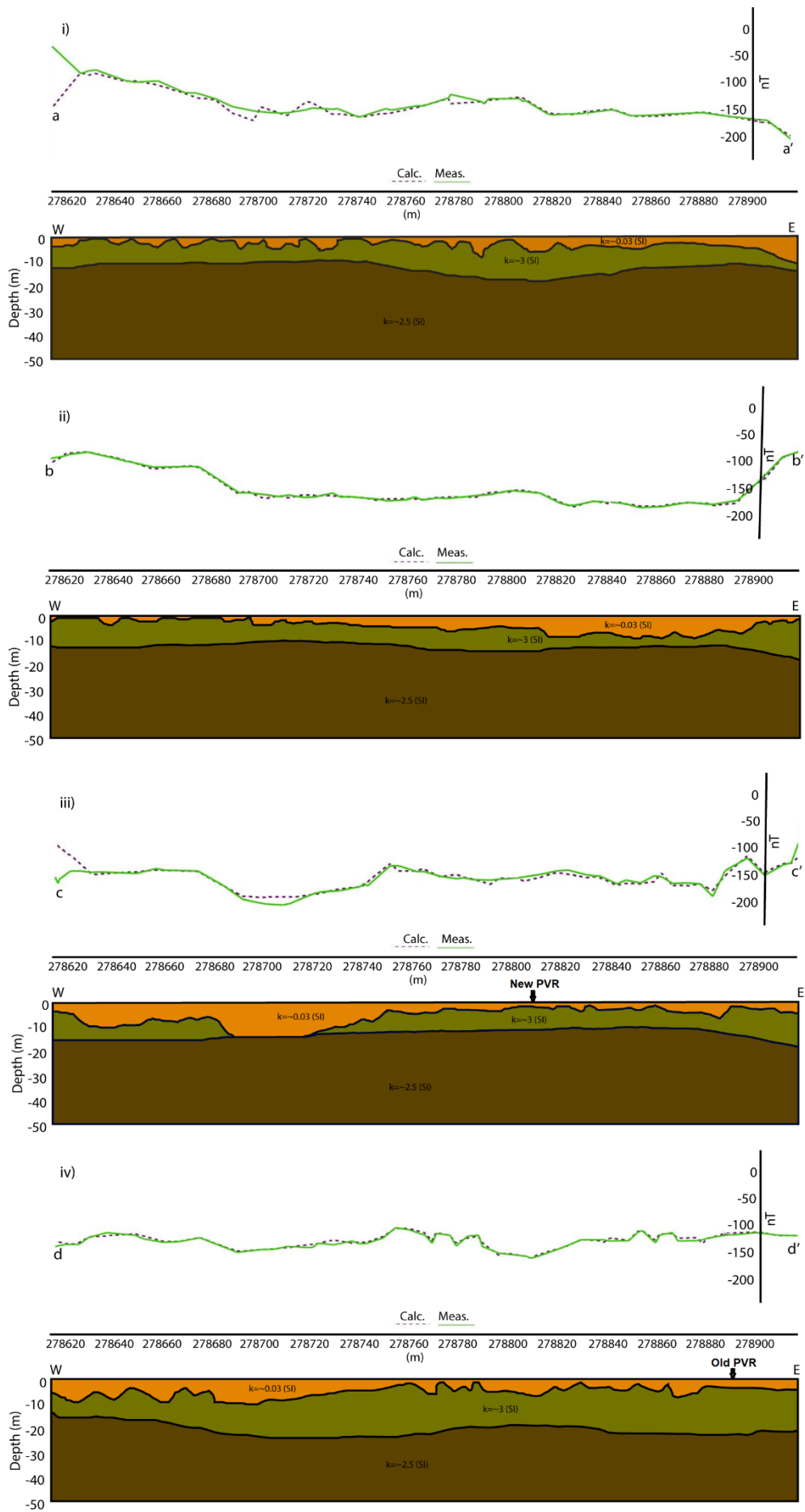
Figure 12: Magnetic data modelling across the profiles i) aa', ii) bb', iii) cc' and iv) dd' incorporating constrain from power spectrum, and past ERT studies. Top, middle and bottom layers in the models are sandy regolith, saprolite and granitic basements. The marked arrows show the location of New and Old PVR in profile cc' and dd'.

iv)   Correlation with conductivity data/information

The cc' magnetic profile is close to the vertical resistive cross-section along AA' of Maurya et al., (2021) where resistivity increases from surface to depth (Figure 13a). The old surface and apparent resistivity data of the region is digitized from the Sanker Narayan et al., (1967) and overlaid over the topography (Figure 13b, 13c). The apparent resistivity shows lateral varying high resistivity outward and vice-versa inside the Choutuppal campus (Figure 13c). This indicates that conductivity decreases outward, highlighting the presence of conductive soil layers within the campus.

The calculated saprolite depth by inverting magnetic data at different locations are ~ 15.5 m (new PVR), ~ 15 m (ABS Room and CH9), ~ 13 m (MB and SP), ~14 m (old PVR, CH5, CH6, CH7), ~ 14.5 m (CH4) (Figure 11a). Whereas, depth estimation by the ERT data are ~ 13.5 m (new PVR), ~ 18 m (ABS Room), ~ 15 m (CH9), ~ 14 m (MB, SP and CH4), ~22 m (old PVR and CH6), ~ 29 m (CH5) ~ 17 m (CH7) respectively (Figure 13e). The calculated depth from these two different datasets show a discrepancy of ~ 2m except at the locations of CH5, CH6 and old PVR. The ERT survey estimates the upper fissured layer depth (~ 9 to 33 meters) of the Choutuppal campus and shows the undulated interface creating compartmentalised aquifers (Nicolas et al., 2019).

428

Figure 13: a) A resistivity model of the 2019 profiles along AA', DD', EE', FF', and GG' and a depth slice at 30m below ground level (after Maurya et al., 2021), b) apparent resistivity, c) surface resistivity superimposed over the topography with lightning strike

location (+ symbol, intensity of 23208 ampere at a distance of 400 m from the MB on 04th May, 2022), d) depth estimation of saprolite interface from ERT data (after Nicolas et al., 2019), e) 3D view of saprolite interface. The blue and red dotted rectangles represent the areas corresponding to the resistivity model and the saprolite interface, respectively, while the black rectangle highlights the magnetic anomaly region.

5. Discussion and conclusion: proposed optimal location for SVR

The high resolution magnetic data provide a detailed shallow sub-surface structure at the CPL observatory. The power spectrum result shows two segments at a depth of ~ 12 m and ~1 m corresponding to saprolite and sandy regolith interface. These depths are similar to the previous depth estimated using the drilling data by Dewandel et al., (2006). The inversion results show the depth variation of the saprolite interface ~ 12 to 16 m (Figure 11a) which underestimate with the upper fissured layer depth from the ERT survey (Figure 13d). The obtained interface shows depression in the central region of the map with crests in the outer region and linear variation in depths (Figure 11a). The estimated depths at different locations shows ~ 2 m differences from these two datasets except at the location of CH5, CH6 and old PVR. These discrepancies in the depths estimation may be due to measurements of two different independent physical parameters susceptibility and conductivity. The saprolite interface might be delineate better by the ERT data due to presence of significant resistivity contrast between saprolite and granitic bedrock in the region (Robinson et al., 2008; Gourdol et al., 2021). The tilt depth plot of the anomaly data reflects depth variation from ~ 2 m to 45 m (Figure 10b). The histogram plot confirms the presence of the shallow sources in the depth range of ~ 2 m to 20 m based on the majority of a number of depth solutions (Figure 10c). These shallow sources are in circular and elongated shapes which may be residue of igneous intrusion (Gorczyk and Vogt, 2018). At shallow depths, circular bodies with a magnetic contact source might produce symmetric

462   anomalies in the magnetic data (Hinze et al., 2013). In contrast, elongated bodies may

463   produce linear magnetic anomalies that follow the direction of the body as in the

464   present study.

465

466   The sub-surface susceptibility models along the magnetic profiles aa', bb', cc', and dd'

467   reflect the geometry of sandy regolith, saprolite layer and basement fissured granite

468   (Figure 12). The saprolite layer shows undulating variation with quiet thick and thin at

469   different locations along the profiles. These variations illustrate that the saprolite layer

470   is thin in the region where the anomaly is low and it shows the thickness in the region

471   where the anomaly is high. The magnetic anomaly shows a large depression of length

472   ~ 80 m in the profile cc' where saprolite layer is absent and this depression arises due

473   to sandy layer in the model. The 3D cross-sectional resistivity model infers the

474   presence of high conductive anomalies followed by the moderate conducting saprolite

475   layer and the low conductive basement rocks (Figure 13a).

476

477   Figure 13c shows that the apparent resistivity increases laterally outward, indicating

478   the presence of highly conductive soil layers within the campus (Sanker Narayan et

479   al., 1967). The apparent and surface resistivity demonstrate the linear relationship with

480   the topography. The comparison between the latest resistivity model (~200 Ωm

481   variation) for 2019 profiles (Figure 13a) and the old apparent resistivity (~300 Ωm

482   variation) plot in 1964 (Figure 13c) shows the resistivity change of ~100 Ωm. This

483   discrepancy may be due to the presence of newly constructed artificial recharge pond

484   which may decrease the resistivity due to its high conductive nature. The thin saprolite

485   layer may be associated with high electrical conductivity, which can result in a low

486   magnetic anomaly, and vice versa. Overall, the resistivity variation increases from

487 surface to greater depth. The resistivity model also show that the artificial recharge

488 pond has good subsurface connectivity, helping the groundwater recharge towards the

489 north and northwest directions in the campus (Maurya et al., 2021). The water level

490 started to rise in June-2016 and reached to very shallow depth in channels during

491 December 2017. It is evident that since last half of 2016, the recharge has led to

492 saturation, which transformed the hydrogeological regime of the campus. This may

493 also cause a partial change in the rock magnetism due to water saturation (Csontos

494 et al., 2019) resulting in a decrease in the magnetic anomaly (Figure 4a, 8a). The

495 rainfall of 2017 monsoon combined with the already prevalent saturated conditions led

496 to the flooding of the magnetometer vault. The location of new PVR has advantages

497 as it is away from the water recharge pond, minimal magnetic anomaly but generation

498 of induced current in the rainy seasons due to presence of conductive environment

499 around the location. The effect of lightning strikes on the data with increasing distance,

500 intensity and ground conductivity shows that higher intensity strikes has had an impact

501 of the data and instruments.

502

503 Based on the above it is very crucial to determine the location and configuration where

504 the installation can avoid the effects of groundwater fluctuations as well as lightning

505 strikes, based on the nature of subsurface rocks, soil conditions, and their magnetic

506 variations. The susceptibility model along with resistivity information are used to make

507 a selection of a new SVR (78.9185E, 17.2939N), indicated by red star in Figures 1, 8,

508 11, 13. This location is on low magnetic anomaly of ~ -145 nT (Figure 8a), resistivity

509 ~200 Ωm (Figure 13a), moderately high ground ~367 m (Figure 13b), and depth of

510 saprolite layer ~ 20 m (Figure 13d). A thicker saprolite layer can enhance the resistive

511 environment and reduce current propagation. The location's sufficient distance (~ 320

m) from the recharge tank ensures that water infiltration is unlikely to pose a significant issue. It is proposed that the pillar will be constructed within a semi-underground vault, in order to minimize the influence of induced currents during rainy seasons and lightning strikes. Additionally, the volume surrounding the pillar should be filled using high-resistivity material, such as Quartzite, to further minimize the likelihood of induced currents during lightning events or wet conditions.

Acknowledgements:

We thank the Director, NGRI, for supporting the work; reference no. NGRI/Lib/2025/Pub-35. The authors are thankful to Dr. Subhash Chandra and other colleagues from the ground water department of CSIR-NGRI for providing the bore well water level data and resistivity results. We also thank Dr. Phani Chandrasekhar and Dr. Rahul Prajapati for help towards the repeat surveys.

Authors' contributions:

DD: Conceptualization, Methodology, Computation and Modeling, Formal analysis, Writing-original draft and editing

SY: Data Processing, Modeling

KA: Conceptualization, Validation, Review and final editing

RM: Lightning data analysis, maps and figures

AT: Lightning data, validation

Declaration of Competing Interest:

The authors declare that they have no competing financial interests or personal relationships that could have appeared to influence the work reported in this paper.

Funding:

No funding was provided for this work.

Availability of data and material

The magnetic data associated with this research are available and can be obtained upon the request from corresponding author. The topography data is obtained from the Shuttle Radar Topography Mission (SRTM) Global 30 (https://earthexplorer.usgs.gov/). The lightning data can be accessed through the ISRO - National Remote Sensing Centre, Hyderabad (https://bhuvan-app1.nrsc.gov.in/lightning/).

References:

Anikiev, D., Götze, H.-J., Plonka, C., et al., 2023. IGMAS+: Interactive Gravity and Magnetic Application System. GFZ Data Services. https://doi.org/10.5880/GFZ.4.5.IGMAS.

Arora K., Chandrashakhar Rao K., Manjula L., et al., 2016. The new magnetic observatory at Choutuppal, Telangana, India. Journal of Indian Geophysical Union, Special volume-2, 67-75.

Arora K., Selles A., Manjula L., et al., 2017. CPL Magnetic Observatory: Groundwater flooding and Relocation requirement. Technical Report No. NGRI-magObs-2017-946.

Chamoli A., Pandey A.K., Dimri V.P., et al., 2011. Crustal configuration of the northwest Himalaya based on modeling of gravity data. Pure and Applied Geophysics 168 (5), 827–844.

561 Chamoli A., Rana S.K., Dwivedi D., et al., 2023. Crustal structure and fault geometries

562 of the Garhwal Himalaya, India: Insight from new high-resolution gravity data modeling

563 and PSO inversion. Tectonophysics, 859, 229904.

564 https://doi.org/10.1016/j.tecto.2023.229904.

565 Csontos A., Kónya P., Falus G., et al., 2019. Unstable spatial differences of the

566 geomagnetic elements caused by changing water saturation of a volcanic

567 sediment. Annals of Geophysics, 61(6), GM669. https://doi.org/10.4401/ag-7351

568 Dewandel B., Lachassagne P., Wyns R., et al., 2006. A generalized 3-D geological and

569 hydrogeological conceptual model of granite aquifers controlled by single or

570 multiphase weathering. Journal of Hydrology, 330, 260-284,

571 https://doi.org/10.1016/j.jhydrol.2006.03.026.

572 Dewandel B., Maréchal J.C., Bour O., et al., 2012. Upscaling and regionalizing

573 hydraulic conductivity and effective porosity at watershed scale in deeply weathered

574 crystalline aquifers. Journal of Hydrology, 416–417, 83-97.

575 https://doi.org/10.1016/j.jhydrol.2011.11.038.

576 Dwivedi D., Chamoli A., Pandey A.K., 2019. Crustal structure and lateral variations in

577 Moho beneath the Delhi fold belt, NW India: Insight from gravity data modeling and

578 inversion. Physics of the Earth and Planetary Interiors, 297, 106317.

579 https://doi.org/10.1016/j.pepi.2019.106317

580 Dwivedi D., Chamoli A., 2021. Source Edge Detection of Potential Field Data Using

581 Wavelet Decomposition. Pure and Applied Geophysics,

582 https://doi.org/10.1007/s00024-021-02675-5.

583 Dwivedi D., Chamoli A., 2022. Seismotectonics and lineament fabric of Delhi fold belt

584 region, India. Journal of Earth System Science, 131, 74.

585 https://doi.org/10.1007/s12040-022-01829-w.

586   Gorczyk W., Vogt K., 2018. Intrusion of magmatic bodies into the continental crust:

587   3D numerical models. Tectonics, 37, 705–723. https://doi.org/10.1002/2017TC004738

588   Gourdol L., Clément R., Juilleret J., et al., 2021. Exploring the regolith with electrical

589   resistivity tomography in large-scale surveys: electrode spacing-related issues and

590   possibility. Hydrology and Earth System Sciences, 25, 1785–1812,

591   https://doi.org/10.5194/hess-25-1785-2021, 2021.

592   Guihéneuf N., Boisson A., Bour O., et al., 2014. Groundwater flows in weathered

593   crystalline rocks: Impact of piezometric variations and depth-dependent fracture

594   connectivity. Journal of Hydrology, 511, 320–334.

595   https://doi.org/10.1016/j.jhydrol.2014.01.061.

596   Hinze W.J., Von Frese R.R.B., Von Frese R., et al., 2013. Gravity and Magnetic

597   Exploration: Principles, Practices, and Applications. Cambridge University Press,

598   Cambridge.

599   Kumar R., Bansal A. R., Anand S. P., et al., 2018. Mapping of magnetic basement in

600   Central India from aeromagnetic data for scaling geology. Geophysical Prospecting,

601   66, 226–239.

602   Maréchal J. C., Selles A., Dewandel B., et al., 2018. An observatory of groundwater in

603   crystalline rock aquifers exposed to a changing environment: Hyderabad, India.

604   Vadose Zone Journal, 17, 180076, https://doi.org/10.2136/vzj2018.04.0076

605   Maurya V.P., Chandra S., Sonkamble S., et al., 2021. Electrically inferred subsurface

606   fractures in the crystalline hard rocks of an Experimental Hydrogeological Park,

607   Southern India. Geophysics, 86(5), WB9-WB18, https://doi.org/10.1190/geo2020-

608   0327.1

609   Miller H. G., Singh V., 1994. Potential field tilt-a new concept for location of potential

610   field sources. Journal of Applied Geophysics, 32, 213–217.

611 Mishra D., Pedersen L.B., 1982. Statistical analysis of potential fields from subsurface

612 reliefs. Geoexploration, 19, 247–265. https://doi.org/10.1016/0016-7142(82)90030-8.

613 Nicolas M., Bour O., Selles A., et al., 2019. Managed Aquifer Recharge in fractured

614 crystalline rock aquifers: Impact of horizontal preferential flow on recharge dynamics.

615 Journal of Hydrology, 573, 717-732, https://doi.org/10.1016/j.jhydrol.2019.04.003.

616 Parker R., 1973. The rapid calculation of potential anomalies. Geophysical Journal

617 International, 31 (4), 447-455, https://doi.org/10.1111/j.1365-246X.1973.tb06513.x

618 Pham L.T., Oksum E., Gómez-Ortiz D., et al., 2020. MagB_inv: A high performance

619 Matlab program for estimating the magnetic basement relief by inverting magnetic

620 anomalies.   Computers   &   Geosciences,   134,104347,

621 https://doi.org/10.1016/j.cageo.2019.104347

622 Reynolds J., 1997. An Introduction to Applied and Environmental Geophysics, Wiley,

623 Chester, 2nd edition, 710p.

624 Robinso D. A., Binley A., Crook N., et al., 2008. Advancing process-based watershed

625 hydrological research using near-surface geophysics: A vision for, and review of,

626 electrical and magnetic geophysical methods, Hydrological Processes, 22, 3604–

627 3635, 2008.

628 Salem A., Williams S., Fairhead J., et al., 2007. Tilt-depth method: a simple depth

629 estimation method using first-order magnetic derivatives. Leading Edge 26, 1502–

630 1505.

631 Sanker Narayan, 1964. Establishment of a magnetic observatory at NGRI. Bull NGRI,

632 2, 115-122.

633 Sanker Narayan P.V., Ramanujachary K.R., Sarma S.V.S., et al., 1967. Establishment

634 of a geoelectric observatory by the NGRI, Hyderabad, at Choutuppal, Nalgonda, Bull.

635 NGRI, 5, 155.

636 Sarma Y.S., Sanker Narayan P.V., Ramanujachary K.R., et al., 1969. Three component

637 induction magnetometer for recording geomagnetic micropulsations at the Geoelectric

638 observatory at Choutuppal, Bull. NGRI, 7, 51-65.

639 Spector A., Grant F.S., 1970. Statistical models for interpreting aeromagnetic data.

640 Geophysics 35 (2), 293–302.

641 Svendsen K.L., Davis W.M., McLean S.J., Meyers, H. 1990. A report on geomagnetic

642 observatory operations. NOAA, NGDC, Boulder, Colorado, USA.

643 Taori A., Suryavanshi A., Pawar S., et al., 2022. Establishment of lightning detection

644 sensors network in India: generation of essential climate variable and characterization

645 of cloud-to-ground lightning occurrences. Natural Hazards, 111, 19-32,

646 https://doi.org/10.1007/s11069-021-05042-8

647 Taori A., Suryavanshi A., Bothale R.V., 2023. Cloud-to-ground lightning occurrences

648 over India: seasonal and diurnal characteristics deduced with ground-based

649 lightning detection sensor network (LDSN). Natural Hazards, 116, 4037-4049.

650 https://doi.org/10.1007/s11069-023-05839-9

651 Telford W. M., Geldart L. P., Sheriff R. E., 1990. Applied Geophysics (2nd ed.).

652 Cambridge: Cambridge University Press.

653 Tiwari V.M., Vyghreswara Rao M.B.S., Mishra D.C., et al., 2006. Crustal structure

654 across Sikkim, NE Himalaya from new gravity and magnetic data. Earth and Planetary

655 Science Letters, 247, 61-69, https://doi.org/10.1016/j.epsl.2006.03.037.